



Engineering cationic defects in transparent tin oxide superlattices

Zhemi Xu, Adnan Younis, Claudio Cazorla *, Jiabao Yi *, Dewei Chu *, Sean Li

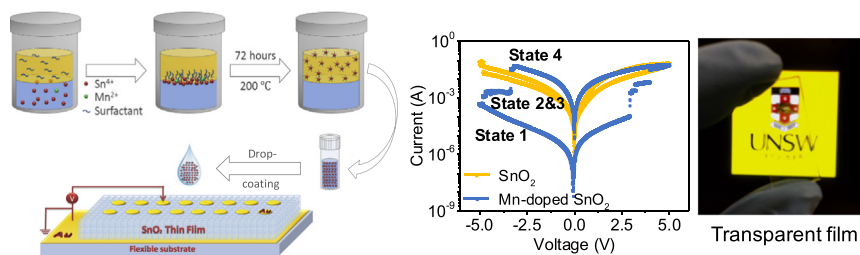
School of Materials Science and Engineering, University of New South Wales, Sydney, NSW 2052, Australia



HIGHLIGHTS

- The defect formation energies in Mn-doped SnO₂ was studied, and it is found that Mn³⁺ occupies the interstitial sites.
- A liquid-liquid interface approach to fabricate SnO₂ thin films through self-assembly technique has been developed.
- Up to 4 nonvolatile resistance states have been achieved via controlling migrations of Mn defects in SnO₂ thin films.

GRAPHICAL ABSTRACT



ARTICLE INFO

Article history:

Received 7 February 2018
 Received in revised form 27 May 2018
 Accepted 28 May 2018
 Available online 28 May 2018

Keywords:

Nanocrystal growth
 Self-assembly
 Tin oxide
 Liquid liquid interface

ABSTRACT

The lack of understanding in engineering cation defects in metal oxides has impeded the development of high performance, and transparent electronic devices. Through studying the formation energy of various cationic defects in Mn-doped SnO₂ via simulation, we found Mn³⁺ cations occupy the interstitial sites of SnO₂ nanocrystals, and we proved that such defects can be engineered to significantly improve resistive switching performance of tin oxide-based devices. With this finding, a new solution-processed approach has been developed to synthesize Mn-doped SnO₂ nanocrystals with a self-assembly technique for high quality transparent Mn-doped SnO₂ thin film fabrication. Defect migration behavior of the Mn-doped SnO₂ thin film was studied by building a metal-oxide-metal sandwich device. The effects of cationic defects, such as Mn interstitials, on the charge transport behavior were further studied to reveal the underlying mechanism. This study provides new insights into the design and engineering of defects in transparent oxides for high-density data storage applications.

© 2018 Elsevier Ltd. All rights reserved.

1. Introduction

With the increasing demand of flexible, transparent and multifunctional electronic devices, transitional metal oxide thin films have attracted extensive research interests because of their high compatibility with complementary metal-oxide-semiconductor (CMOS) technology [1–3]. Recently, various transparent metal oxides including ZnO [4], SnO₂ [5], In₂O₃ [6] and TiO₂ [7] have been widely explored for applications in thin film transistors [8,9], non-volatile memories [10,11], and gas sensors [12,13]. In applications, manipulation of oxygen vacancies is

often considered as one of the most important approaches for tuning the optical and electrical properties of transparent metal oxides [14,15]. However, the absence of systematic investigations on the role of cationic defects in transparent metal oxides has limited further optimization of their physical properties for practical applications. This is because the modification of the concentration of oxygen vacancies only results in a small range of variation of electrical conductivity and optical transparency [16]. Hence, it is of importance to understand the effects of cationic defects on the electronic and optical properties of transparent metal oxides in order to manipulate the physical properties of metal oxides in innovative ways.

SnO₂ is a metal oxide with multifunctional properties and it has been widely used in many electronic devices [13,17,18]. Currently, SnO₂ thin film is generally prepared by physical and chemical vapour deposition

* Corresponding authors.

E-mail addresses: c.cazorla@unsw.edu.au, (C. Cazorla), jiabao.yi@unsw.edu.au, (J. Yi), d.chu@unsw.edu.au (D. Chu).

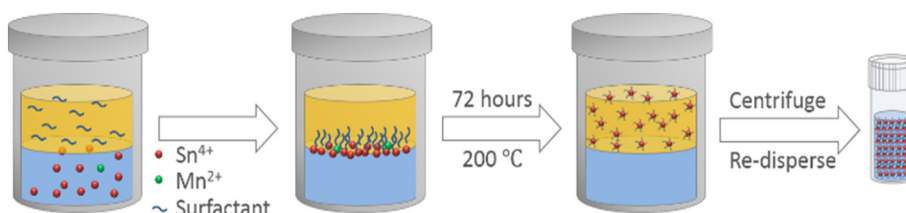


Fig. 1. Schematic diagram for the self-assembly SnO_2 nanoparticle synthesis by liquid-liquid interface reaction.

techniques, such as magnetron sputtering [19], pulsed laser deposition (PLD) [20] and chemical vapour deposition (CVD) [21]. Although high-quality films have been fabricated with these technologies, the scale of the as-fabricated films has been limited by the vacuum chamber. In addition, the processes are expensive and complex. Hence, to develop a simple and cost-effective fabrication process, such as a printable technique based on solution processing, becomes very important. However, the fabrication of high-quality SnO_2 thin film devices through chemical synthesis without post annealing is a challenge due to the low crystallization rate at a relatively low processing temperature. In addition, it is also critical to control the hydrolysis of precursors for achieving the desired particle size and shape [22].

Recently, liquid-liquid interface reactions has been used for synthesizing self-assembled thin film with homogeneous oxide nanoparticles via a controllable nucleation and growth procedure near the liquid-liquid interface for electronic applications [23,24]. In this paper, we present a new approach to control the size and self-assembly of SnO_2 nanoparticles through the liquid-liquid interface reaction. Meanwhile, the effects of the dopants and doping levels on the defect distribution have been systematically investigated.

To reveal the underlying mechanisms of the observed physical phenomena, the possibilities of cationic vacancy formation in SnO_2 have been studied. Theoretical and experimental results presented in this work demonstrate that the optical and electrical properties of transparent oxide thin films can be efficiently optimized through engineering cation defects, hence paving the way towards the realization of high-performance storage devices.

2. Experimental procedure

2.1. Materials synthesis and device fabrication

SnO_2 nanocrystals were synthesized through a solvothermal process as shown in Fig. 1. 15 mL of a $16.7 \text{ mmol}\cdot\text{L}^{-1}$ Tin (IV) chloride pentahydrate ($\text{SnCl}_4\cdot\text{H}_2\text{O}$) aqueous solution was added as a raw solution into a 50 mL autoclave. Then, a mixed solution of toluene (15 mL), oleic acid (OLA, 0.8 mL), and tert-butylamine (0.1 mL) was added to the autoclave carefully to achieve the liquid-liquid interface between these two solutions. To synthesize Mn-doped SnO_2 , Manganese (II) chloride was added in the 15 mL aqueous solution by 6.25 mol% and 12.5 mol% to form Mn-doped SnO_2 respectively. All chemicals were purchased from Sigma-Aldrich. The sealed autoclave was heated to 200°C for 72 h and then cooled down to room temperature for 90 min. Then the upper organic solution was centrifuged to acquire the pure and Mn-doped SnO_2 nanocrystals. The centrifuged SnO_2 nanocrystals were re-dispersed into 0.3 mL of toluene. Finally, the re-dispersed SnO_2 solution was ready for thin film deposition. In the drop coating process, $8 \mu\text{L}$ solution was dropped on a 2 cm^2 Au-coated silicon for each layer and followed by 20 min UV light treatment with a 254 nm wavelength UV light. The drop coating followed by the UV treatment was repeated for 3 times to allow a thicker film deposition. To form a dry and uniform thin film, the final film was treated with UV light for another 4 h.

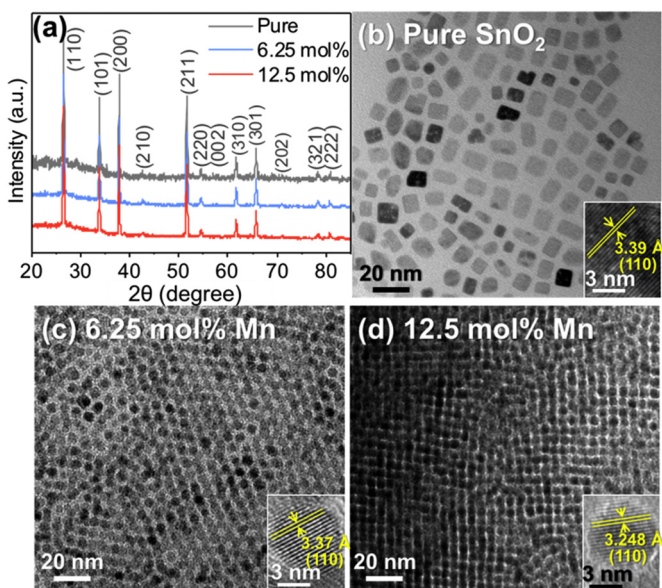


Fig. 2. (a) X-Ray diffraction patterns; (b), (c) and (d) TEM and HRTEM (inset) images of pure SnO_2 , self-assembly 6.25% and 12.5% Mn-doped SnO_2 .

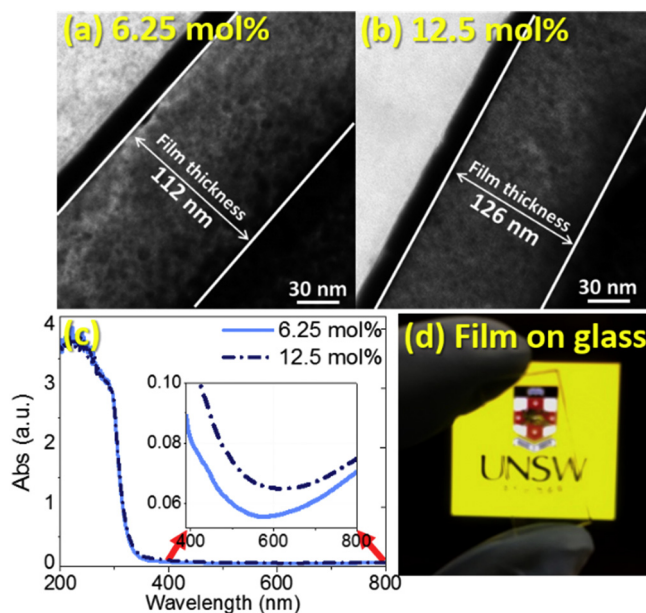


Fig. 3. (a) and (b) TEM images (cross-section) of 6.25% and 12.5% Mn-doped SnO_2 thin films; (c) UV-vis spectrum of 6.25% and 12.5% Mn-doped SnO_2 films on glass; (d) the transparent 12.5 mol% Mn-doped SnO_2 thin film on glass.

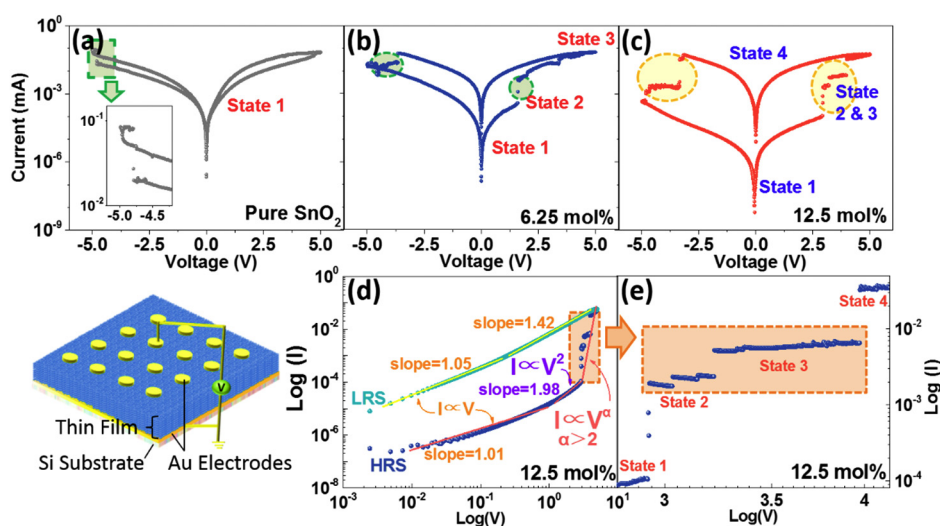


Fig. 4. I–V measurements of (a) pure SnO₂, (b) 6.25% and (c) 12.5% Mn-doped SnO₂; I–V curves in log–log scales of (d) 12.5% Mn-doped SnO₂ thin film and (e) the enlarged region.

2.2. Characterization

The structural analysis of the fabricated SnO₂ nanocomposite was carried out using an X-ray diffraction (XRD) system (Philips X'pert Multipurpose X-ray Diffraction System (MPD) with Cu K α radiation). Transmission electron microscopy (TEM) investigations were carried out by a Philips CM200 microscope. X-ray photoelectron spectroscopy (XPS) was tested by Thermo Scientific ESCALAB250Xi. The pass energy was 20 eV for region scans. The electrical properties characteristics were measured using an Autolab 302 N electrochemical workstation controlled with Nova software. The SnO₂ thin film was deposited on gold-coated Si and patterned gold top electrode (diameter: 250 μ m) were coated on the top as top electrodes for voltage–current curve measurements. All electrical measurements were performed in air at room temperature.

3. Results and discussion

3.1. Synthesis of self-assembled nanoparticles

SnO₂ and Mn-doped SnO₂ nanoparticles were synthesized using a liquid–liquid interface approach and subsequently deposited on glass substrates for the characterization by X-ray diffraction (XRD). Fig. 2(a) shows XRD spectra of the pure SnO₂ and Mn-doped SnO₂ thin films with doping level of 6.25 mol% and 12.5 mol% respectively (JCPDS #41-1445). No Mn related impurity phase was detected, which shows Mn has been successfully doped into SnO₂ lattice.[25] The normalized (110) peaks of SnO₂ shifted to higher angles by increasing Mn-doping level, as shown in supporting information Fig. S-1. This peak shifting

may be attributed to the internal stress caused by the defects induced by Mn doping [26].

TEM images of the un-doped SnO₂, 6.25 mol% and 12.5 mol% Mn-doped SnO₂ nanoparticles are shown in Fig. 2(b), (c) and (d), respectively. The individual nanoparticles were found to be single-crystalline. The d-spacing of (110) plane for the un-doped, 6.25% and 12.5% doped SnO₂ were calculated as 0.339 nm, 0.337 nm and 0.325 nm respectively, as shown in Fig. 2 (c) and (d). This decrease in d-spacing with Mn doping indicates the increased stress level induced by Mn doping, which also matches well with XRD results. The average size of 6.25 mol% Mn-doped SnO₂ nanoparticles is ~6.14 nm while the 12.5 mol% Mn-doped SnO₂ is ~5.36 nm. The detail size distribution analysis is provided in supporting information Table S-1. A high degree of self-assembly can essentially form high-quality thin films.

3.2. Uniform, dense and transparent thin film

TEM and UV–vis photospectroscopy were implemented to characterize film uniformity, film density and transparency as shown in Fig. 3. The TEM images of cross-sectional Mn-doped SnO₂ thin films are shown in Fig. 3(a) and (b). The thicknesses of both thin films were found as 112 and 126 nm with a relatively smooth and flat surface. UV–Vis absorption spectra shown in Fig. 3(c) demonstrate the Mn-doped SnO₂ films have a strong absorption for the wavelength shorter than 350 nm, evidencing that they are transparent to the visible light as shown in Fig. 3(d). Mn-doped SnO₂ shows good transparency with over 90% visible light transmittance, making it suitable for transparent electronic devices.

3.3. Multi-level resistance states by manipulating Mn-doping concentrations

To investigate the Mn-doping effects on resistance states in SnO₂ thin film, current–voltage characteristics of the SnO₂ films are illustrated in Fig. 4. The I–V curves are plotted in Fig. 4(a) to (c) with the voltage sweeping mode of 0 \rightarrow 5 \rightarrow 0 \rightarrow -5 \rightarrow 0 V. During all measurements, the voltage was applied on the top electrode, while keeping bottom electrode as ground as illustrated in Fig. 4. In the inset of Fig. 4(a), the pure SnO₂ film shows a small gap between resistance states, while the 6.25 mol% and 12.5 mol% Mn-doped SnO₂ exhibit a larger gap between different resistive states. As shown in Fig. 4(b) and (c), the current in 6.25 mol% and 12.5 mol% Mn-doped SnO₂ film jumped from relatively low to a higher level at switching voltages of 1.57 V and 2.73 V, respectively. In the reverse voltage sweep direction, similar phenomena

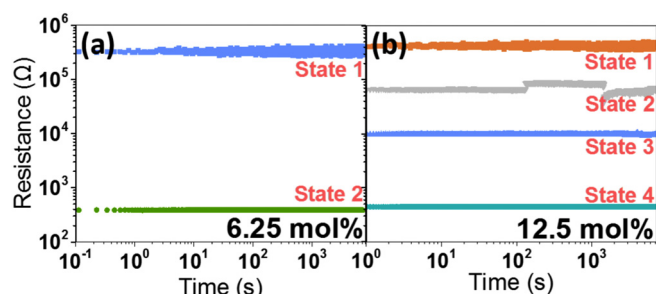


Fig. 5. Retention tests of (a) 6.25% and (b) 12.5% Mn-doped SnO₂ for 7200 s.

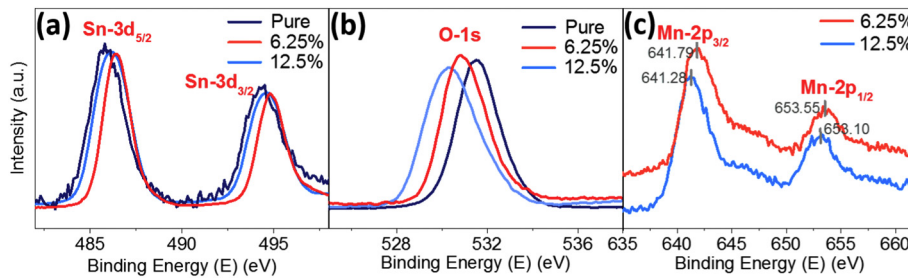


Fig. 6. XPS spectra of Mn-doped SnO₂ thin film for (a) Sn 3d, (b) O 1 s and (c) Mn2p.

occurred at -3.65 V (6.25 mol%) and -3.19 V (12.5 mol%). More importantly, the 12.5 mol% Mn-doped SnO₂ thin film showed multi-step back transition in resistance instead of one-step transition. The first transition appeared at 2.95 V to the intermediate states 2 and 3 and then the final state 4 at 4.07 V. Although similar behavior was also observed in the 6.25 mol% thin film (marked State 2), the intermediate state in the 6.25 mol% thin film is not stable in retention tests as provided in supplementary Fig. S-2 (a). To further analyze the current voltage characteristics of 12.5 mol% Mn-doped SnO₂ thin film, the I–V curve was replotted in log-log scales as shown in Fig. 4(d). In both pure and Mn-doped SnO₂ thin films, the first stage, where $I \propto V$, corresponds to the space charge limited conduction (SCLC) process which refers to an ohmic conduction behavior.[27] However, the conduction phenomena appeared in the HRS of the 12.5% Mn-doped SnO₂ is complex as shown in Fig. 4(d). Three distinct I–V regions are identified: (1) the ohmic relationship ($I \propto V$ from 0 to 0.54 V), (2) the region between 0.54 V and 2.39 V corresponds to the Child's law ($I \propto V^2$) from and (3) the steep current increasing region [28,29].

The enlarged 'steep current increasing region' is provided in Fig. 4 (e). The discontinuity of I–V characteristics results in two separated I–V segments, thus inducing two remarkable resistance states, marked as State 2 and State 3. The retention tests for the individual materials were conducted and the results were plotted in Fig. 5. It shows the resistance states are stable for over 7200 s at room temperature. The retention tests for the pristine SnO₂ thin film were also measured and shown in Supplementary Fig. S-2 (b). As shown, the resistance states ratios were low. It is of interest to note that the pristine SnO₂, by increasing the Mn-doping concentration in SnO₂, the resistance states increased to two [Fig. 5(a)] and then four resistance states [Fig. 5(b)]. It suggests that the transport behavior of SnO₂ thin film can be controlled by manipulating the Mn-doping level in SnO₂. The question is: what plays the dominant role in inducing the multi-level resistance states needs to be clarified?

3.4. Identification of the specific defects in Mn-doped SnO₂

Our findings above give rise to the questions: (1) Dose this unique behaviour only appear in Mn-doped SnO₂ film? and (2) what is the mechanism underlying the observed multi-level resistance states? To answer the aforementioned questions, it is essential to analyze the valence states of Mn in SnO₂ and then compare other elements doping with the same state, as Mn is a transition metal with various valence states. The XPS spectra of the Mn 2p, Sn 3d and O 1s are plotted in

Table 1
Energy values, difference between Mn and SnO₂ valence band top energy levels.

Mn-doping concentration (mol%)	Energy values (eV)				Mn peak doublet separation (eV)
	Mn 2p _{3/2}	Mn 2p _{1/2}	Sn 3d _{5/2}	Sn 3d _{3/2}	
Pure	–	–	485.83	494.36	–
6.25	641.88	653.40	486.59	495.02	11.52
12.5	641.40	65,291	486.10	494.55	11.51

Fig. 6. Table 1 summarizes the data obtained through XPS. The high-resolution spectra show that the binding energies of Sn 2p_{5/2} and 2p_{3/2} are ~ 486 eV and ~ 495 eV and that of O 1 s is ~ 530 eV for all the films. The doublet energy separation values between the Sn 3d_{5/2} and 3d_{3/2} are ~ 8.4 eV, which agrees well with the theoretical value of Sn⁴⁺ in SnO₂ (Δ is 8.41 eV) [26]. When the Mn-doping concentration increases, the shifts towards lower energy side in binding energy is triggered by the decreasing of SnO₂ size with Mn-doping [30], which is in good agreement with the TEM and calculation analysis. The detailed XPS spectra of O1s are shown in Fig. 6(b) and the binding energy of O1s is around 530 eV, which is corresponding to the lattice oxygen in Mn-doped SnO₂ [26,31].

The binding energy core levels of Mn 2p_{3/2} in 6.25 mol% and 12.5 mol% Mn-doped SnO₂ peaked at 641.88 eV and 641.40 eV, and Mn 2p_{1/2} peaked at 653.40 eV and 652.91 eV, respectively. The energy difference between Mn 2p_{3/2} and Mn 2p_{1/2} is ~ 11.5 eV. Such results agree with reported data [26,32], showing that the doped Mn is most likely in the Mn³⁺ state [31,33]. Compared to 6.25 mol%, the Mn-2p peaks in 12.5 mol% shift more to lower binding energy, which indicates that with increasing Mn-doping concentration, the concentration of Mn at lower charge states increases. XPS spectra are consistent with the presence of Mn³⁺ substituting Sn⁴⁺ in SnO₂. In this case, to maintain the charge neutrality, the cationic defects should be formed.

To confirm this hypothesis, formation energy calculations of point defects in Mn-doped SnO₂ were performed by using first-principles methods based on density functional theory (DFT). To understand the nature of cationic defects as induced by Mn doping, we estimated the formation energy of all possible point defects and of pairs of point defects in Mn-doped SnO₂ with first-principle methods. The formation energies of each point defects are plotted in Fig. S-3 in supporting information. The relative oxygen chemical potential represents the oxygen concentration in the synthesis environment, and low potential means less oxygen in the system. It is shown that, in Sn-rich/O-poor condition in Fig. S-3, the defect pair of Mn substitution at Sn site (Mn_{Sn}) and Mn interstitials in SnO₂ lattice (Mn_{int}) has the lowest formation energy. Thus, Mn³⁺ is possible to maintain the charge neutrality by forming extra Mn_{int} in the lattice. However, such defects can only form in low oxygen concentration conditions.

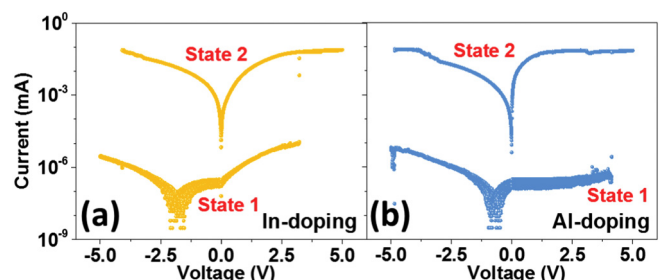


Fig. 7. I–V measurements of 12.5% (a) In-doped and (b) Al-doped SnO₂.

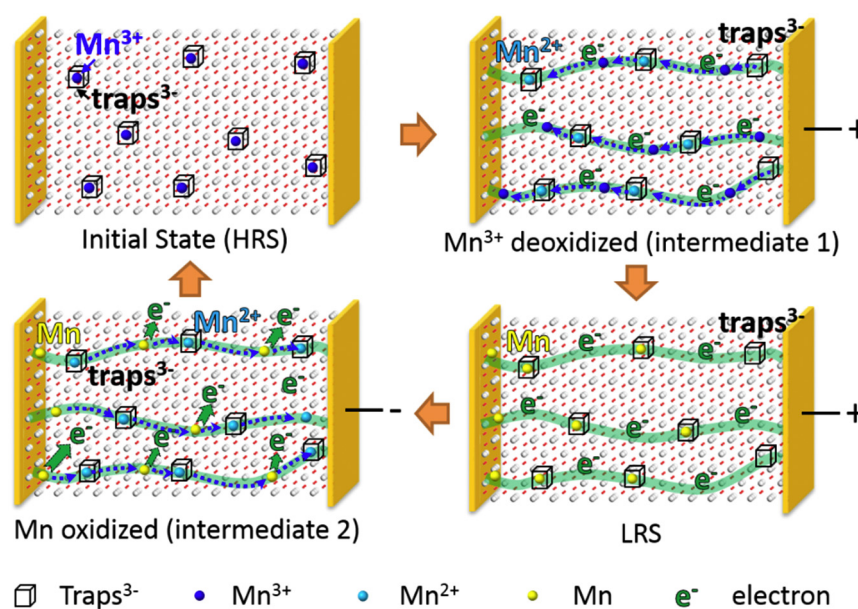


Fig. 8. Schematics of Mn_{int} induced multi-level resistive switching process.

3.5. Possibilities of achieving multi-level states by other X³⁺ element doping

To further confirm the contribution of Mn-doping, it is necessary to compare with other dopants. Although Mn is a multi-valence element, the main valence in this work is 3+ according to the XPS analysis. Thus, other trivalent ions, such as Al and In were used to verify the effects of Mn on the observed transport behavior.

12.5 mol% Al-doped and In-doped SnO₂ samples were also fabricated by keeping all other parameters same and their I–V curves are plotted in Fig. 7(a) and (b). Compared to the pristine SnO₂ thin film shown in Fig. 4(a), the distinct transition of I–V behaviors is observed in the range of both 0–5 V and –5 to 0 V sweeping process. However, different from the Mn-doped SnO₂ (Fig. 4(c)), there is no intermediate states appeared in these materials. Fig. S-4 shows the plots of I–V curves in a log-log scale. Similar to 12.5 mol% Mn-doped SnO₂, both the ohmic region ($I \propto V$) and the Child's law region ($I \propto V^2$) are found in the In-doped and Al-doped SnO₂ thin films. Differently, the steep current increase region in Fig. 4(d) is absent, indicating that the multi-level resistance states cannot be achieved by Al and In dopants, although the remarkable transitions between LRS to HRS are observed. Thus, it is reasonable to identify that the X³⁺ doping is not the key that induced multi-level resistance states in SnO₂.

3.6. Possible switching mechanism

According to previous report [34], in both Al and In-doping in SnO₂, defects of interstitials have high formation energies. This means that as compared to Mn-doped SnO₂ the barriers of forming interstitials are higher in Al-doped and In-doped SnO₂. However, the interstitials are weakly bonded in the crystal lattice, thus these defects can contribute into redox reactions much easier than the substitutions, which may give rise to a resistance state transition. Based on the above results, we proposed a possible mechanism of achieving multi-level resistance states in Mn-doped SnO₂ thin film. The underlying mechanism of I–V characters induced by Mn³⁺ redox is illustrated in Fig. 8.

Initially, the thin films are in HRS. By increasing sweep voltage, the resistance of Mn-doped SnO₂ thin films gradually transit from HRS to LRS (as in Fig. 5). Such a transition is related to the Mn_{int}³⁺ migration towards cathodes. The Mn_{int}³⁺ migrates to cathodes, receives electrons and is reduced to Mn²⁺ and then to Mn, which switches Mn-doped SnO₂ to

the intermediate state. In the 6.25 mol% and 12.5 mol% Mn-doped SnO₂ thin films, the first resistance state changed at +1.57 V and +2.73 V, respectively as shown in Fig. 4(b) and (c). The results agree with previous reports [35] that the redox potentials for Mn³⁺ to Mn²⁺ in aqueous solutions is +1.54 V. It is reasonable that higher potential is needed in Mn-doping concentration to fully reduce Mn³⁺ to Mn²⁺. With the accumulation of deoxidized Mn, filaments formed by Mn from cathodes to anodes, switched the film to LRS. When positive voltage applied, the Mn releases electrons and is oxidized to Mn³⁺. The positively charged Mn³⁺ gradually migrates away from anodes, jump back to Mn³⁺ traps, and switches the film to the initial state.

The multi-intermediate states in 12.5 mol% was triggered by the different charged Mn_{int} states. According to XPS, although Mn³⁺ dominates the Mn charge state, the 12.5 mol% doped SnO₂ contains lower charged Mn_{int} than 6.25 mol%. The lower charged Mn_{int} can be reduced when a relatively small voltage applied, achieving the State 2 in Fig. 4(c). Then, with higher voltage applied, Mn³⁺ is reduced, switched the film to the State 3. After being fully switched on, positive voltage can oxidize Mn to lower charge states and with increasing the applied voltage, the film is switched to HRS again.

4. Conclusions

In this work, we have analyzed the formation of cationic defects in SnO₂ and found theoretically that Mn interstitials can be induced through tuning the doping level. Experimentally, with a new liquid-liquid interface method, well controlled Mn-doped SnO₂ nanocrystal arrays were synthesized and transparent thin films were fabricated. Owing to the existence of Mn_{int} defects, multi-state, non-volatile transport under electric field was confirmed. In addition, the mechanism of how the type and distribution of cationic defects affect the electrical properties of the thin films was studied. These results may provide significant new insights into the design and engineering of transparent metal oxides, which are desirable for information storage device applications.

Acknowledgement

This work was supported by the Australian Research Council Project of FT140100032, FT140100135, DP150103006, and DP140104373.

Appendix A. Supplementary data

Supplementary data to this article can be found online at <https://doi.org/10.1016/j.matdes.2018.05.061>.

References

- [1] A. Liu, R. Jones, L. Liao, D. Samara-Rubio, D. Rubin, O. Cohen, R. Nicolaescu, M. Paniccia, A high-speed silicon optical modulator based on a metal–oxide–semiconductor capacitor, *Nature* 427 (6975) (2004) 615–618.
- [2] Y.-C. Ye, T.-J. King, C. Hu, Metal-dielectric band alignment and its implications for metal gate complementary metal–oxide–semiconductor technology, *J. Appl. Phys.* 92 (12) (2002) 7266–7271.
- [3] K.-H. Shen, S.-H. Chen, W.-T. Liu, B.-H. Wu, L.-J. Chen, Effective Schottky barrier lowering of Ni silicide/p-Si (100) using an ytterbium confinement structure for high performance n-type MOSFETs, *Mater. Des.* 114 (2017) 220–225.
- [4] E.M. Fortunato, A. Pimentel, A. Gonçalves, A. Marques, L. Pereira, R. Martins, Fully transparent ZnO thin-film transistor produced at room temperature, *Adv. Mater.* 17 (5) (2005) 590–594.
- [5] Z. Xu, P. Guan, A. Younis, D. Chu, S. Li, Manipulating resistive states in oxide based resistive memories through defective layers design, *RSC Adv.* 7 (89) (2017) 56390–56394.
- [6] G. Palmer, K.R. Poeppelmeier, T.O. Mason, Conductivity and transparency of ZnO/SnO₂-cosubstituted In₂O₃, *Chem. Mater.* 9 (12) (1997) 3121–3126.
- [7] A. Krumpmann, J. Dervaux, L. Derue, O. Douhéret, R. Lazzaroni, R. Snyders, A. Decroly, Influence of a sputtered compact TiO₂ layer on the properties of TiO₂ nanotube photoanodes for solid-state DSSCs, *Mater. Des.* 120 (2017) 298–306.
- [8] K.-H. Lim, J. Lee, J.-E. Huh, J. Park, J.-H. Lee, S.-E. Lee, Y.S. Kim, A systematic study on effects of precursors and solvents for optimization of solution-processed oxide semiconductor thin-film transistors, *J. Mater. Chem. C* 5 (31) (2017) 7768–7776.
- [9] L. Wu, H. Gao, X. Zhang, An experimental investigation on the effective electron mass in InGaO₃ (ZnO) 3 by valence electron energy-loss spectroscopy, *Mater. Des.* 95 (2016) 410–413.
- [10] D.O. Schmidt, S. Hoffmann-Eifert, H. Zhang, C. La Torre, A. Besmehn, M. Noyong, R. Waser, U. Simon, Resistive switching of individual, chemically synthesized TiO₂ nanoparticles, *Small* 11 (48) (2015) 6444–6456.
- [11] I. Hilmi, A. Lotnyk, J.W. Gerlach, P. Schumacher, B. Rauschenbach, Epitaxial formation of cubic and trigonal Ge-Sb-Te thin films with heterogeneous vacancy structures, *Mater. Des.* 115 (2017) 138–146.
- [12] L. Li, C. Zhang, W. Chen, Fabrication of SnO 2–SnO nanocomposites with p–n heterojunctions for the low-temperature sensing of NO 2 gas, *Nano* 7 (28) (2015) 12133–12142.
- [13] A. Facchetti, T. Marks, *Transparent Electronics: From Synthesis to Applications*, John Wiley & Sons, 2010.
- [14] C.T. Campbell, C.H. Peden, Oxygen vacancies and catalysis on ceria surfaces, *Science* 309 (5735) (2005) 713–714.
- [15] A. Nadarajah, M.E. Carnes, M.G. Kast, D.W. Johnson, S.W. Boettcher, Aqueous solution processing of F-doped SnO₂ transparent conducting oxide films using a reactive Tin(II) hydroxide nitrate Nanoscale cluster, *Chem. Mater.* 25 (20) (2013) 4080–4087.
- [16] H. Hosono, Recent progress in transparent oxide semiconductors: materials and device application, *Thin Solid Films* 515 (15) (2007) 6000–6014.
- [17] C.-H. Huang, J.-S. Huang, C.-C. Lai, H.-W. Huang, S.-J. Lin, Y.-L. Chueh, Manipulated transformation of filamentary and homogeneous resistive switching on ZnO thin film memristor with controllable multistate, *ACS Appl. Mater. Interfaces* 5 (13) (2013) 6017–6023.
- [18] J. Lin, Z. Peng, C. Xiang, G. Ruan, Z. Yan, D. Natelson, J.M. Tour, Graphene nanoribbon and nanostructured SnO₂ composite anodes for lithium ion batteries, *ACS Nano* 7 (7) (2013) 6001–6006.
- [19] T. Minami, H. Nanto, S. Takata, Highly conducting and transparent SnO₂ thin films prepared by RF magnetron sputtering on low-temperature substrates, *Jpn. J. Appl. Phys.* 27 (3A) (1988) L287.
- [20] Y. Suda, H. Kawasaki, J. Namba, K. Iwatsuji, K. Doi, K. Wada, Properties of palladium doped tin oxide thin films for gas sensors grown by PLD method combined with sputtering process, *Surf. Coat. Technol.* 174 (2003) 1293–1296.
- [21] J. Jeong, S.-P. Choi, C.I. Chang, D.C. Shin, J.S. Park, B. Lee, Y.-J. Park, H.-J. Song, Photoluminescence properties of SnO₂ thin films grown by thermal CVD, *Solid State Commun.* 127 (9) (2003) 595–597.
- [22] C. Ribeiro, E.J. Lee, T.R. Girdali, E. Longo, J.A. Varela, E.R. Leite, Study of synthesis variables in the nanocrystal growth behavior of tin oxide processed by controlled hydrolysis, *J. Phys. Chem. B* 108 (40) (2004) 15612–15617.
- [23] A. Younis, D. Chu, C.M. Li, T. Das, S. Sehar, M. Manefield, S. Li, Interface thermodynamic state-induced high-performance memristors, *Langmuir* 30 (4) (2014) 1183–1189.
- [24] C.-L. Xu, Y.-Z. Wang, Self-assembly of stearic acid into nano flowers induces the tunable surface wettability of polyimide film, *Mater. Des.* 138 (2018) 30–38.
- [25] C.-H. Lee, D.-J. Choi, Y.-J. Oh, Characterization of the p-type Sn_{1-x}Mn_xO₂ oxide semiconductor nanoparticles by sol-gel method, *Electron. Mater. Lett.* 9 (3) (2013) 283–286.
- [26] B. Venugopal, B. Nandan, A. Ayyachamy, V. Balaji, S. Amirthapandian, B.K. Panigrahi, T. Paramasivam, Influence of manganese ions in the band gap of tin oxide nanoparticles: structure, microstructure and optical studies, *RSC Adv.* 4 (12) (2014) 6141–6150.
- [27] Q. Liu, W. Guan, S. Long, R. Jia, M. Liu, J. Chen, Resistive switching memory effect of Zr O 2 films with Zr+ implanted, *Appl. Phys. Lett.* 92 (1) (2008), 012117 .
- [28] M.A. Lampert, P. Mark, *Current Injection in Solids*, 1970.
- [29] Y. Sharma, P. Misra, R.S. Katiyar, Unipolar resistive switching behavior of amorphous YCrO₃ films for nonvolatile memory applications, *J. Appl. Phys.* 116 (8) (2014), 084505 .
- [30] Y. Tay, S. Li, C. Sun, P. Chen, Size dependence of Zn 2p_{3/2} binding energy in nanocrystalline ZnO, *Appl. Phys. Lett.* 88 (17) (2006) 173118.
- [31] S. Lekshmy, S. Nair, V.S.N. Anitha, P.V. Thomas, K. Joy, Magnetic properties of Mn-doped SnO₂ thin films prepared by the sol-gel dip coating method for dilute magnetic semiconductors, *J. Am. Ceram. Soc.* 97 (10) (2014) 3184–3191.
- [32] M. Herrera, D. Maestre, A. Cremades, J. Piqueras, Growth and characterization of Mn doped SnO₂ nanowires, nanobelts, and microplates, *J. Phys. Chem. C* 117 (17) (2013) 8997–9003.
- [33] A. Ungureanu, C. Andronescu, G. Voicu, A. Scoban, O. Oprea, N. Stanica, I. Jitaru, Structural characterisation and luminescence properties of paramagnetic Mn doped SnO₂ nanopowders obtained via simple butanol assisted sol-gel synthesis, *Dig. J. Nanomater. Biostruct.* 8 (3) (2013) 1169–1178.
- [34] D.O. Scanlon, G.W. Watson, On the possibility of p-type SnO₂, *J. Mater. Chem.* 22 (48) (2012) 25236–25245.
- [35] K.S. Yamaguchi, D.T. Sawyer, The redox chemistry of manganese (III) and-(IV) complexes, *Isr. J. Chem.* 25 (2) (1985) 164–176.